Flow design and simulation of a gas compression system for hydrogen fusion energy production

EJ Avital[1], E Salvatore[1], A Munjiza[2], V Suponitsky[3], D Plant[3], M Laberge[3]

[1]School of Engineering and Materials Science, Queen Mary University of London, Mile End Rd London E1 4NS, UK

[2]Civil Engineering, University of Split, Livanjska 2100 Split, Croatia

[3]General Fusion Inc., 108-3680 Bonneville Place, Burnaby, BC V3N 4T5, Canada

An innovative gas compression system is proposed and computationally researched to achieve short time response as needed in engineering applications as hydrogen fusion energy reactors and high speed hammers. The system consists of a reservoir containing high pressure gas connected to a straight tube which in turn is connected to a spherical duct, where at the sphere's centre plasma resides in the case of a fusion reactor. Diaphragm located inside the straight tube separates the reservoir's high pressure gas from the rest of the plenum. Once the diaphragm is breached the high pressure gas enters the plenum to drive pistons located on the inner wall of the spherical duct that will eventually end compressing the plasma. Quasi-1D and axisymmetric flow formulations are used to design and analyse the flow dynamics. A spike is designed for the interface between the straight tube and the spherical duct to provide a smooth geometry transition for the flow.

Flow simulations show high supersonic flow hitting the end of the spherical duct, generating a return shock wave propagating upstream and raising the pressure above the reservoir pressure as in the hammer wave problem, potentially giving temporary pressure boast to the pistons. Good agreement is revealed between the two flow formulations pointing to the usefulness of the quasi-1D formulation as a rapid solver. Nevertheless, a mild time delay in the axisymmetric flow simulation occurred due to moderate two-dimensionality effects. The compression system is settled down in a few milliseconds for a spherical duct of 0.8 m diameter using Helium gas and uniform duct cross-section area. Various system geometries are analysed using instantaneous and time history flow plots.

Keywords: Gas compression, shock wave, flow simulation, fusion energy

List of symbols

A	- duct's cross section area
a	- local speed of sound
a_0, a_1, a_2	- coefficients in the spikes radial polynomial function (Appendix A)
b	- co-volume equation of state (EOS) parameter
E	- total energy per unit density
h	- duct's width, see Fig 1
p	- static pressure
p_0	- stagnation pressure
M	- Mach number
R	- radius in spherical co-ordinates
R_{sph}	- radius of the inner wall of the spherical duct, see Fig 1
r	- radius in cylindrical co-ordinates
r_m	- radius of the duct's median line, see Fig 1
r_t	- radius of the straight tube, see Fig1
s	- co-ordinate that follows the duct's median line, see Fig 1
t	- time
u	- velocity along the duct's median line, see Fig 1
v_x	- axial velocity in cylindrical co-ordinates
v_r	- radial velocity in cylindrical co-ordinates
x	- axial co-ordinate in cylindrical co-ordinates
x_e	- axial location of the end of the spherical duct's inner wall, see Fig 1
x_t	- axial location of the start of the trim of the end of the spherical duct.
x_{sph}	- axial location of the centre of the sphere forming the spherical duct, see Fig 1
x_0	- axial location of the diaphragm, see Fig 1
x_1	- axial location of the front end of the spike, see Fig 1
x_2	- axial location of the spike's streamwise grid line merging with the spherical duct, Fig 1
α	- FORCE scheme positive integer
β	- normalized distance of streamwise grid line from the inner wall (Appendix A)
β_{trim}	- trim coefficient for the end of the spherical duct (Appendix B)
θ	- spherical angle, see Fig 1
ρ	- static density
ψ	- TVD function limiter

1. Introduction:

The goal of producing sustainable hydrogen fusion energy has attracted significant interest in the last 50 years. This goal has raised many engineering challenges where simulations have a significant role in providing valuable insight into the physical processes and paving the way towards efficient development of fusion energy systems. Recently, a promising design has been proposed, using the concept of the Magnetized Targeted Fusion (MTF) reactor by General Fusion Inc. It combines the use of strong magnetic fields for controlling the plasma and fluids compression to achieve the ignition of the plasma and sustaining the fusion reaction [1]. A significant obstacle is the very short lifespan of the plasma measured up to milliseconds by which it must be ignited. One possible way is to inject the magnetized plasma into a cavity inside a spinning liquid shell and then to collapse this shell compressing the plasma trapped inside. This method is attractive due to the high speed of sound of the liquid and the ability to match the acoustic impedance of the liquid to that of the outer wall of the reactor by choosing liquid metal for the spinning liquid shell inside the reactor. Thus one can use pneumatic pistons mounted outside the reactor to send compression waves through the spinning liquid metal that will in turn compress the plasma [2]. However, this method introduces new challenges such as the energy efficiency of the liquid compression and the complex dynamics of liquid-gas interface [3]. In this study we research an alternative compression system that can potentially achieve the goal of effective compression in time scale of milliseconds by releasing highly pressurized gas into a closed enclosure of very low pressure. Such method can also be attractive for other applications requiring rapid compression as high speed detonators and hammers.

The release of high pressure gas into nearly vacuum conditions has already attracted the attention of the space engineering sector for propulsion purposes [4]. Flow computations based on characteristics arguments and computational fluid dynamics (CFD) were pursued, and where interestingly quasi-1D flow assumptions were commonly used due to the low computational cost [4, 5]. However, the system proposed in this study differs significantly from the space propulsion systems by having the high pressure gas expanding into a closed enclosure and not free space. This introduces new challenges in terms of the simulation and analysis of the flow development.

A schematic description of the researched system is given in Fig 1. A reservoir of highly pressurized gas is connected to a straight tube which in turn is connected to a spherical duct. The spherical duct encloses a spherical space where the plasma resides. Very low pressure gas resides in the spherical duct and is separated from the high pressure gas by a diaphragm. At a certain time the diaphragm is breached and the high pressure gas expands into the straight tube and then into the spherical duct. Array of pistons mounted on the inner wall of the spherical duct will accelerate inwards by the high pressure gas. Those pistons initially placed in contact with liquid metal, will push liquid metal

toward the center of the sphere forming an imploding shell which in turn compresses the plasma. Such design has been inspired by the design of the LINUS fusion power plant where reservoirs of high pressure gas are to drive pistons that will compress liquid-metal liners [6]. However, the proposed design differs in geometry and in the use of gas allowing it to expand into a plenum which subsequently leads to driving pistons for compressing the plasma. As a result the gas reservoir pressure in this design is high as 1000 bars while in the LINUS design it is 200 bars.

The compression system illustrated in Fig. 1 resembles the classic shock tube problem [7], although it differs in its geometry and the closed end of the spherical duct. The shock tube flow analysis shows the generation of a shock wave as well as an expansion wave. Occurrence of shock waves must be reduced in the current design in order to reduce energy losses and the time it takes to achieve high pressure gas in the duct. Such shocks can also interfere with the valves located on the inner side of the spherical duct. Therefore a very low pressure gas is assumed to exist in the spherical duct before the diaphragm is breached in order to reduce as much as possible the initial shock wave caused by the compression of the very low gas as the high pressure gas expands into the enclosure. A spike is placed at the junction between the spherical duct and the straight tube as seen in Fig. 1 in order to provide smooth transition between those two sections, so to eliminate or at least reduce shock waves that may occur at that junction area. This results in design requirements for the spike to be assessed using the flow simulations.

To simplify this study only the flow development is simulated where other engineering considerations such as structural integrity, control of the diaphragm breach and the pistons located on the inner side of the spherical duct are left for future studies. Thus the walls of both the straight tube and spherical duct are assumed to be rigid and the diaphragm is assumed to be entirely breached instantly as in the classic shock tube problem. The simulations methodology is presented next, followed by the aerodynamic design of the spike, results and analysis of full size compression systems with various initial conditions and summary.

2. Flow simulation methodology

The governing equations for the flow development are taken as the compressible Euler equations. This means that the effect of viscosity is neglected. It is justified by the very short time scales of the flow development not allowing viscosity effect to become significant. It follows similar arguments that were made for the cryogenic shock tube [8]. It is also taken that the assumption of flow continuum is valid. This is accurate for the high pressure gas but is probably not for the low pressure gas that resides in the spherical duct before the breach of the diaphragm. However, our interest is in the high pressure gas and we assume low pressure gas in the spherical duct just to mimic the effect of

near zero pressure on the front of the high pressure gas as it expands into the spherical duct. Such simulation approach is also commonly used to simulate water surface motion by including a section of the air above the water in the simulation [9].

Two sets of governing equations are used. The first is of the quasi-1D flow assumption and the second is of axisymmetric flow assumption. While the latter is more accurate, the quasi-1D flow equations provide the fundamentals for the spike design and rapid flow calculations, and as already noted before it is commonly used in the propulsion industry.

2.1 Quasi-1D flow formulation

The quasi-1D inviscid flow governing equations are as follows [5, 10];

$$\frac{\partial \rho}{\partial t}+\frac{\partial(\rho u)}{\partial s}+\frac{\rho u}{A}\frac{dA}{ds}=0 \quad , \tag{1}$$

$$\frac{\partial(\rho u)}{\partial t}+\frac{\partial(\rho u^2+p)}{\partial s}+\frac{\rho u^2}{A}\frac{dA}{ds}=0 \quad , \tag{2}$$

$$\frac{\partial(\rho E)}{\partial t}+\frac{\partial[(\rho E+p)u]}{\partial s}+\frac{(\rho E+p)u}{A}\frac{dA}{ds}=0 \quad . \tag{3}$$

Eqs. (1), (2) and (3) are the continuity, momentum and energy equations respectively. ρ is the density, u is the flow velocity along the co-ordinate s that follows the duct's median line, ρE is the total energy and p is the pressure. A is the cross-section area of the duct. One can take $A=2\pi r_m h$, where r_m is the radial distance of the duct's median line from the axis of symmetry and h is the duct's width, see Figure 1.

The co-volume equation of state (EOS) is used to close the system of equation. It is a simple generalisation of the perfect gas EOS, accounting for real gas effects at very high pressures, e.g. up to a compression of air to a destiny of about 2000 kg/m^3 [8]:

$$E=\frac{1}{2}u^2+\frac{p(1-b\rho)}{\rho(\gamma-1)},\ a^2=\frac{\gamma p}{(1-b\rho)\rho} \quad . \tag{4}$$

b is a small positive number that may depend on the density, γ is the ratio of specific heats and a is the local speed of sound. Taking b=0 leads to the perfect gas EOS.

The time marching of Eqs. (1) to (3) is achieved using the mid-point (second order) Runge-Kutta method, where a time fractional approach is used to march first the convection terms, i.e. the terms with the spatial first derivative of the flow property. These terms are calculated using the 1st order FORCE scheme that is applicable for the compressible Euler equations with an arbitrary EOS [10]. A superbee-type TVD scheme is used to improve the spatial accuracy to second order, yielding the FLIC (TVD-FORCE) scheme [10]. The source terms (those with a derivative dA/ds in Eqs. (1) to (3)) are marched using a semi-implicit or a Crank-Nicholson approach for every sub time step of the

Runge-Kutta scheme. Such procedure is illustrated for the continuity equation when marching from time stage n to n+1/2 as part of the Runge-Kutta time marching;

$$\frac{\rho^o-\rho^n}{\Delta t}=-\frac{F^n_{i+1/2}-F^n_{i-1/2}}{\Delta s} \quad , \tag{5}$$

$$F^n_{i+1/2}=F^{FORCE}_{i+1/2}+\psi\left(F^{LW}_{i+1/2}-F^{FORCE}_{i+1/2}\right) , \; F^{FORCE}_{i+1/2}=\frac{1}{2}\left(F^{LW}_{i+1/2}+F^{LF}_{i+1/2}\right) \quad , \tag{6}$$

where ψ is the TVD limiter function and

$$F^{LF}_{i+1/2}=\frac{(\rho u)^n_{i+1}+(\rho u)^n_i}{2}-\frac{\Delta s}{2\alpha\Delta t}\left(\rho^n_{i+1}-\rho^n_i\right) \quad , \tag{7}$$

$$F^{LW}_{i+1/2}=\widetilde{(\rho u)}_{i+1/2}=\frac{1}{2}[(\rho u)^n_i+(\rho u)^n_{i+1}]-\frac{\alpha\Delta t}{2\Delta s}[(\rho u^2+p)^n_{i+1}-(\rho u^2+p)^n_i] \quad , \tag{8}$$

where the momentum equation (2) was used to derive the right hand side of Eq (8). α is a positive integer, the higher it is the less dissipative but less stable the FORCE scheme is. Toro [10] recommended α=(1,2,3) for (1D,2D,3D) simulations respectively. In our simulations α=2 was found to be sufficient. Finally

$$\frac{\rho^{n+1/2}-\rho^o}{\Delta t}=-0.5\frac{\rho^{n+1/2}+\rho^n}{A}u^n\frac{dA}{ds} \quad . \tag{9}$$

u^n is replaced by $u^{n+1/2}$ at the second time step of the Runge Kutta method to achieve second order accuracy in time. An alternative analytical method to march Eq. (9) is illustrated at the next sub-section for the axisymmetric simulations.

The boundary conditions at the end of the spherical duct are taken as of an adiabatic wall. The open end of the straight tube into the reservoir at *x*=0 in Fig. 1, requires caution. At early time it should allow the high pressure gas from the reservoir to enter the tube but at later times it should allow gas to leave the tube if an over-pressure has been built up inside the tube (e.g. in case of a shock wave). Thus an inflow/outflow condition has been implemented using the following strategy:

a. First assume a zero velocity gradient at the inflow and find velocity at *x*=0.

b. If the velocity is positive, limit it up to the local speed of sound assuming no flow separation causing a venturi effect, use the reservoir's properties, the steady 1D energy equation by assuming the time scales inside the tube are much shorter than in the reservoir [11], and the EOS to calculate the incoming flow properties.

c. If the velocity is negative, use characteristic outflow condition with a semi- empirical correction for an incoming characteristic to account for the effect of the reservoir's pressure [12].

2.2 Axisymmetric flow formulation

The axisymmetric (2D) inviscid flow equations are written in cylindrical coordinates [13];

$$\frac{\partial \rho}{\partial t}+\frac{\partial(\rho v_r)}{\partial r}+\frac{\partial(\rho v_x)}{\partial x}=-\frac{\rho v_r}{r} \quad . \tag{10}$$

$$\frac{\partial(\rho v_r)}{\partial t}+\frac{\partial(\rho v_r^2+p)}{\partial r}+\frac{\partial(\rho v_x v_r)}{\partial x}=-\frac{\rho v_r^2}{r} \quad . \tag{11}$$

$$\frac{\partial(\rho v_x)}{\partial t}+\frac{\partial(\rho v_r v_x)}{\partial r}+\frac{\partial(\rho v_x^2+p)}{\partial x}=-\frac{\rho v_r v_x}{r} \quad . \tag{12}$$

$$\frac{\partial(\rho E)}{\partial t}+\frac{\partial[(\rho E+p)v_r]}{\partial r}+\frac{\partial[(\rho E+p)v_x]}{\partial x}=-\frac{(\rho E+p)v_r}{r} \quad . \tag{13}$$

v_r and v_x are the velocities in the radial (r) and axial (x) directions receptively. Eqs. (10) to (13) are supplemented by EOS (4).

The unstructured FORCE formulation has been applied for quadrilateral elements [10], accounting for the curvature of the spherical part of the enclosure. The super-bee TVD formulation was used to convert the formulation to FLIC and bring it to second order accuracy. As in the quasi- 1D formulation, a fractional time step approach was used where the fluxes on the left hand side of Eqs. (10) to (13) were treated using the FLIC (TVD-FORCE) approach and the right hand sides as sources. This approach is illustrated for the continuity equation (10) when marching from time stage n to n+1/2;

$$\frac{\rho^o-\rho^n}{\Delta t}+\frac{\partial(\rho v_r)^n}{\partial r}+\frac{\partial(\rho v_x)^n}{\partial x}=0 \quad , \tag{14}$$

$$\frac{\rho^{n+1/2}-\rho^o}{\Delta t}=-\frac{\rho v_r^n}{r} \quad . \tag{15}$$

Eq. (14) is marched using the 2nd order FLIC (TVD-FORCE) approach and Eq. (15) can be marched in time using a a Crank-Nicholson approach or analytically as $\rho^{n+1/2}= \rho^o \exp(-v^n_r \Delta t/r)$. The latter is formally of first order accuracy in time because of v^n_r in its expression. However, it can be extended to second order in time using the mid-point Runge-Kutta method by replacing v^n_r with $v^{n+1/2}_r$ at the second sub-time step.

Axisymmetry boundary conditions were implemented on the axis of symmetry. As inviscid flow was assumed due to the very short time scales of the flow, inviscid adiabatic wall boundary conditions were used. A 1D inflow/outflow characteristic boundary condition was implemented at the entrance from the reservoir to the tube (x=0) following the procedure outlined for the quasi-1D flow formalisation. A short buffer zone was implemented just after x=0 to suppress 2D fluctuations at x=0 [14].

3. Design considerations

The two main objectives of the compression system are (i) rapid increase of the (static) pressure inside the spherical duct and (ii) keeping the pressure uniform as much as possible along the inner wall of the spherical duct. This is to prompt a synchronized operation between the pistons located on that wall. For this purpose we can vary the location of the diaphragm, add a spike between the straight tube and the spherical duct, and vary the width of the spherical duct. Obviously we can move forward the diaphragm as close as possible to the spike in order to reduce the time it takes the pressure to build up inside the spherical duct. However, imperfect breach of the diaphragm can cause 3D flow effects inside the spherical duct and reduce the effectiveness of the system. In this study we assume a perfect breach of the diaphragm and thus place it near the front edge of the spike.

The spike itself should provide a smooth transition in the flow cross-section area A between the straight tube and the spherical duct. Following Eqs. (1) to (3) this means continuous A and dA/ds (or dA/dx). A procedure to derive the spike's median line, inner and outer walls is detailed in Appendix A using a family of second order polynomials.

Keeping the spherical duct's width h uniform along the axial direction x will cause a strong variation in the cross- section A with x as $A=2\pi r_m h$, see Fig. 1. This is undesirable as it will increase the time scale of the compression system due to increased volume of the enclosure and will also lead to an unequal operation of the pistons located on the spherical duct's inner wall. This is because there will be different volumes of high pressure gas above the various pistons. Therefore a simple procedure to yield a uniform A along the spherical duct is detailed in Appendix B.

Finally a return shock wave is expected to occur once the high pressure gas hits the end of the spherical duct as the high pressure gas is expected to enter the plenum at supersonic speed. Such return shock wave may cause the pistons over the duct's inner wall to work in a non-synchronized way. In order to reduce the strength of the return shock wave, trimming to the width of the spherical duct can be pursued, i.e. the width is reduced towards the end of the duct. It can make that section work as a convergent section of a nozzle that slows supersonic flow. A simple second order polynomial is also detailed in Appendix B to achieve this trimming.

4. Results and analysis

The quasi-1D and 2D codes noted as *CLithium*1 and *Clithium*2 were verified using several ways and two verification examples are given. Figures 2 and 3 show the two verification examples for air flow, taking $\gamma=1.4$ and b=0 in the EOS (4). The first example is the classical shock tube verification for *Clithium*1 schematically shown in Fig. 2a. The numerical results of the instantaneous pressure distribution are compared with the theoretical solution [7]. The grid resolution is 0.04 m and good

agreement between all numerical results and the theoretical solution is revealed. Using the FLIC (TVD-FORCE) formulation improves the numerical solution at the vicinity of the expansion wave but not as much at the shock wave. This is because a TVD formulation degenerates to a 1st order at a strong jump in the density/pressure.

The second verification example is of a flat-faced cylinder put in a uniform incoming supersonic flow of M=2 that is shown in Fig 3. The Mach contour levels are shown after the flow settled for the FLIC formulation of CLithium2 with α=2, a grid size of (451,451) points and a grid clustering near the axis of symmetry, making the radial step Δr at r=5 m twice of that at r=0. As expected a detached bow shock appears in front of the face of the cylinder, reducing the speed from supersonic to subsonic. The shock wave spreads away from the cylinder as a conical wave. The distance of the normal shock wave from the front of the cylinder is within 6% error compared with experimental results [7]. Further verifications were carried by observing physical behaviour of the flow such as uniform convection at the straight tube of the compression system and fulfilling the Rankine-Hugoniot relationship for a return shock wave in a closed straight tube, i.e. a simplified compression system of a straight tube only.

The following design parameters were set for the compression system; the straight tube radius r_t = 0.2 m, the diaphragm's location x_0 = 0.9 m, the front end of the spike x_1 = 1 m, the spherical radius of the inner wall of the spherical duct R_{sph} = 0.4 m, the centre of the sphere x_{sph} = 1.7 m and the end of the spherical duct's inner wall at x_e = 2.09 m. If trimming was applied to the end of the spherical duct's width, it started at x_t = 1.9 m. The gas was taken as Helium because of its high ambient speed of sound taken as 1010 m/s at reservoir conditions and γ = 1.67. The effect of the co-volume EOS parameter b in Eq. (4) was found to be small using the level of values expected for it [10], thus it was simply taken as zero in the following simulations. All following simulations used the 2nd order FLIC (TVD-FORCE) scheme with α=2.

4.1 Quasi-1D flow analysis

Three geometries were investigated for the compression system as shown in Figs. 4; (a) a uniform spherical duct's cross section area equal to the straight tube's cross-section area, (b) the same as Geometry (a) but where the spherical duct's width is trimmed to zero at the end of the duct, and (c) a uniform spherical duct's width of 0.2 m as the straight tube radius. The instantaneous pressure distributions along the median line of the compression system are shown in Figs. 5 for all three geometries and several time stages, where a grid size of less than 1000 points was found to be sufficient. All cases show at t=0.001 s a small return shock wave evolving after the high pressure gas hits the end of the spherical duct. It is generated by the supersonic nature of the flow as shown by the corresponding instantaneous Mach number distributions plotted in Figs. 6.

As time progresses the return shock wave propagates upstream against the incoming flow, resulting in increase of the pressure difference over the shock wave. Because Geometries (a) & (b) with the uniform cross-section areas have less volume than Geometry (c) with the uniform duct's width, the return shock wave is further upstream for Geometries (a) & (b) than for (c) at the same time stage. One should note that the volume of the duct is accounted by the terms of dA/ds in Eqs (1) to (3) of the quasi-1D flow formulation. The same argument holds for Geometry (b) which has a smaller volume than Geometry (a) due to the trimming of the end of the spherical duct. Thus at t<0.01 s the return shock waves in Geometries (a) & (b) show pressure difference higher than in Geometry (c). However, when we look at the strength of the shock wave, i.e. the pressure difference normalised by the pressure in front of the wave, the picture is opposite and the return shock waves of Geometries (a) & (b) are weaker than of Geometry (c).

This is also evidenced by the Mach numbers shown in Figs. 6 for Geometries (a) & (b) that are lower than for (c). However, one should note that these Mach numbers are for the velocities relative to a stationary observer. The strength of the shock wave is influenced by the velocity of the flow relative to the shock and thus the velocity of the shock wave propagating upstream should be added to the flow velocity in order to get the Mach number for an observer moving with the shock wave. This is why there is still a return shock wave at t=0.01 s in Fig. 5(a), while the flow Mach number relative to a stationary observer is only high subsonic according to Fig 6(a).

To illustrate the effect of the trimmed end of the duct on the return shock wave, a characteristic area rule for a shock wave moving into stationary fluid in a non-uniform tube is utilized from Whitham's [15];

$$\frac{M_{sh}}{M_{sh}^2-1}\lambda\left(M_{sh}\right)\frac{dM_{sh}}{dz}+\frac{1}{A}\frac{dA}{dz}=0 \quad . \tag{16}$$

M_{sh} is the Mach number of the shock relative to the fluid in front of it in the tube, A is the tube's cross-section area and z is the direction of the shock wave propagation. $\lambda(M_{sh})$ is an algebraic function of M_{sh} and it is bounded between 4 to about 5. Although Eq. (16) was derived for a shock moving into stationary fluid unlike our case, we use it qualitatively here following the concept of a Galilean transformation. For our case of a return shock wave, direction z is opposite to x. Hence dA/dz >0 for the trimmed end, leading to a decrease in M_{sh} and thus a decrease in the return shock wave strength.

An interesting effect of the return shock wave is that the pressure behind it rises to almost double the reservoir pressure before settling around the reservoir pressure after the shock wave exited into the reservoir. It is similar to the hammer wave problem where flow in a duct is suddenly stopped by a valve, causing the pressure to rise almost twice the stagnation pressure [11]. This effect can be of

advantage to the design by increasing the pressure to push the pistons located on the inner wall of the spherical duct. However, the transient behaviour of the pressure increase and decrease has to be considered when looking at synchronization between the pistons.

The time it takes the flow to settle down in Geometries (a) & (b) is much lower than in Geometry (c) because of the smaller volumes of Geometries (a) & (b). From Figs. 5, one can see that as the shock wave exited into the reservoir a mild refraction wave propagated back to the enclosure as seen at t=0.01 s for Geometries (a) & (b), while at that time the return shock wave is still inside the compression system for Geometry (c). The differences in the time scales between the three geometries are further illustrated in the pressure time history contours of Fig. 7, where the horizontal axis corresponds to the axial direction and the three regions of straight tube, spike region and spherical duct are marked. The occurrence of the return shock wave is clearly seen in all three plots. In Geometries (a) & (b) the pressure is settling down around the reservoir pressure in the spherical duct region at about t=0.008 s, while in Geometry (c) there is still strong transient behaviour at that region. One should note the smooth transition of the flow in the spike region with no abrupt change of the pressure contour lines for the uniform cross-section area configurations of Geometries (a) & (b). It demonstrates the success of the spike design at least when it comes to the quasi-1D flow analysis.

The pressure distribution along the spherical duct's inner wall are of high importance as they affect the operation of the planned pistons aimed to push liquid metal inwards to create an imploding shell to compress the magnetized plasma residing inside the sphere. The time histories of the pressure at selected points along that wall are shown in Figs. 8 up to t=0.01 s. While the pressure for Geometry (c) still increases at t=0.01 s, it already settled down at that time for the other Geometries as was also seen in Figs. 7. Geometry (a) with its trimmed end of the spherical duct end shows the shortest time scale and first reaches the reservoir pressure in 2 milliseconds. Thus in terms of achieving the lowest time scale, this geometry suits best.

4.2 Axisymmetric flow analysis

As Geometry (c) with its uniform spherical duct's width was shown not to answer the requirements of time scales of milliseconds for the flow to settle down, it was disregarded for this 2D flow analysis. Structured grid of about 1000 points in the streamwise direction and 70 points in the stream-normal direction was found to be sufficient after grid sensitivity study. The grids are illustrated in Figs. 9, where only every tenth in each direction is shown for clarity. The grid is rectangular in the tube region, whereas for the other regions the streamwise grid lines were built using procedures outlined in Appendixes A & B, while keeping the spherical duct's inner wall perfectly spherical. The stream-normal grid lines were built normal to the inner wall yielding a grid

that was close to an orthogonal one. One should note that because of the use of a structured grid, the end of the spherical duct of Geometry (b) could not be trimmed to zero width. This would have resulted in a singularity on the wall where the grid points would have collapsed on the same point to yield a very restrictive CFL limit on the time step. Thus the width of the end of the spherical duct of Geometry (b) was trimmed to 15% of its value in Geometry (a). Practically it is also expected that the width of the spherical duct will be finite because of manufacturing and structural considerations.

The instantaneous pressure contours at t=(0.001, 0.002, 0.003) s are shown in Figs. 10 & 11 for Geometries (a) & (b) respectively. The corresponding instantaneous Mach number contours are shown in Figs. 12 & 13. All reveal the flow behaviour already found by the quasi-1D flow analysis, supersonic flow hitting the end of the spherical duct, generating a return shock wave that propagates upstream against the incoming flow, while increasing the pressure to almost twice the reservoir pressure until exiting into the reservoir. The pressure and Mach numbers levels also correspond well to the levels found by the quasi-1D flow analysis.

However, there are also some discrepancies caused by two-dimensionality in the flow. This is in particular in the spike region during the early stage of the flow entering the spherical duct and when the first return shock wave reaches that region. This is clearly seen by the Mach number contours of Geometry (a) in Figs. 12. It involves the generation of mild oblique shock waves as seen in Figs. 12(b) & (c) which are undesirable as they slow the flow and reduce the stagnation pressure. Additional two-dimensionality is revealed near the end of the spherical duct of Geometry (a) at t=0.001 s, where it widens to keep with the design constraint of a uniform cross-section area. Trimming that end as in Geometry (b) eliminates that two-dimensionality when comparing Fig. 10(a) with Fig. 11(a). It also helped in reducing some of the mild two-dimensionality in the spike region at t=(0.002, 0.003) s as revealed by comparing Figs. 12(b) & (c) with Figs. 13(b) & (c).

Both geometries show two return shock waves at t=0.003 s, one is just before the spike region for Geometry (a) or just after it for Geometry (b), and the second one is still inside the spherical duct. A similar but milder pattern was also found using the quasi-1D flow analysis in Figs. 5. The flow's low Mach number around the second (later) shock wave indicates that it moves faster than the first one. This is illustrated in Figs. 11, where the first shock propagated about a quarter of the spherical duct circumference from t=0.001 s to 0.002 s as seen in Figs 11(a) & (b), while for the second wave it took less than 0.001 s to propagate from the end of the spherical duct to its mid-streamwise location by Figs 11 (b) & (c).

From the design point of view, the most important aspect is the pressure distribution along the inner wall of the spherical duct, where the pistons leading to the sphere's core lay. The time history contours of the pressure along the inner wall of the spherical duct, spike and the tube's axis of

symmetry is shown in Figs. 14 for both geometries. Again the flow pattern is very similar to that revealed by the quasi-1D flow results of Figs. 7. The two-dimensionality in the spike region and at the end of the spherical duct for Geometry (a) causes a small delay in the time scales of the flow when comparing Figs. 7 with 14. As in the case of the quasi-1D flow, analysis of Geometry (b) with its trimmed duct end shows the fastest time scales. The fact the trim did not reduce the duct's width fully to zero had little effect on the flow time scales when comparing Fig. 14(a) of the axisymmetric simulation with Fig. 7(b) of the quasi-1D flow simulation, where the end of the duct's width was trimmed to zero.

The time history of the pressure at selected points along the inner wall of the spherical duct is shown in Figs. 15. When compared with the results of the quasi -1D flow simulations in Figs. 8, it is seen that as a result of the two-dimensionality mentioned earlier, there is a delay of less than 1 millisecond in the time scale of the pressure evolution for both geometries. Nevertheless, the pressure behaviour and level are very similar between the axisymmetric and the quasi-1D flow simulations . For example at t=0.004 s, p is about $1.9p_{0,\text{high}}$ for Geometry (b) by the quasi-1D flow results, while it is $1.86p_{0,\text{high}}$ by the axisymmetric flow results, where $p_{0,\text{high}}$ is the reservoir pressure by Fig. 1. Similarly for Geometry (a) p is about $1.85p_{0,\text{high}}$ at that time by the quasi-1D flow results and $1.80p_{0,\text{high}}$ by the axisymmetric flow results.

5. Summary

An innovative gas compression system aimed at compressing magnetized plasma for hydrogen fusion energy generation and other applications required rapid compression, was suggested and computationally analysed for its flow performance. The system is composed of a reservoir of very high pressure Helium gas connected to a straight tube which in turn is connected to a spherical duct. Pistons mounted on the inner wall of the spherical duct are powered by the high pressure gas once it got to the duct in order to compress plasma at the centre of the sphere in case of a fusion reactor. Design requirements include time scales of no more than a few milliseconds for the pressure to build up in the spherical duct once the diaphragm separating the high pressure gas in the reservoir from the plenum is breached.

Quasi-1D and axisymmetric inviscid flow formulations have been suggested and computationally implemented, where viscosity was neglected due to the very short time scales of the flow. Both formulations were verified against known benchmark problems. The quasi-1D flow formulation was used to design a spike between the straight tube and the spherical duct in order to provide smooth transition between them and avoid strong shock waves that would delay the flow and cause stagnation pressure losses.

Three geometries were investigated for the compression system; (a) with a uniform cross-section area throughout, (b) the same as (a) but with the width of the end of spherical duct gradually trimmed to zero or 15% of its intended value and (c) with a uniform duct's width throughout. All geometries showed a similar flow pattern of a high supersonic flow hitting the end of the spherical duct soon after the diaphragm holding the reservoir gas is breached. This was followed by a return shock wave propagating upstream and as in the hammer wave problem, causing the pressure to temporally rise above the reservoir pressure which can benefit the design, followed by a secondary but faster return shock wave. Once the return shock wave exited into the reservoir, the flow in the entire system settled through series of mild compression and expansion waves.

The good agreement between the quasi-1D flow and axisymmetric flow results demonstrated the usefullness of the quasi-1D flow formulation as a rapid design tool. There were small discrepancies in the pressure levels between the two formulations and the system time scale was longer by less than 1 millisecond in the axisymmetric formulation than in the quasi-1D formation. This was related to two-dimensionality in the flow at the spike region and near the end of the spherical duct, which Geometry (a) had slower response more than of Geometry (b). In overall the time scales of Geometries (b) were the shortest. This was related to its smaller volume but also to the unsteady aerodynamics of the return shock wave at the trimming area near the end of the spherical duct.

This gas compression design can be part of a bigger design for producing hydrogen fusion energy, but because its time scale is in milliseconds it will require careful control and synchronization with other parts of the reactor.

References:

[1] Laberge M (2009), Experimental results for an acoustic driver for MTF, *J. Fusion Energy* **28**(2), 179–182.

[2] Suponitsky V, Froese A, Barsky S (2014), Richtmyer-meshkov instability of a liquid-gas interface driven by a cylindrical imploding pressure wave, *Computers & Fluids* **89**, 1–19.

[3] Suponitsky V, Plant D, Avital EJ, Munjiza A (2015), Propagation of pressure waves in compression system prototype for magnetized target fusion reactor in General Fusion Inc., Proc. 30th Int Symp Shock Waves, Tel-Aviv, Israel, July 19-24.

[4] Takashima Y, Karsahara J and Shepherd JE (2006), Impulse generated by a shock tube in a vacuum, 46th AIAA Aerospace Meeting, Reno

[5] Kopasakis G, Connolly JW, Paxson DE and Woolwine KJ (2012), Quasi 1D modelling of mixed compression supersonic inlets, AIAA paper 2012-0775, 50th Aerospace meeting, Nashville

[6] Turci P (1984), A compact-toroid fusion reactor design at 0.5 Megagauss, based on stabilized liner implosion techniques, 3rd Int Conf Megagauss Magnetic Field Generation Related Topics, Moscow, 184

[7] Liepmann HW and Roshko A (1993), *Elements of gas dynamics*, Dover.

[8] Cummings JC (1974), Development of a high performance cryogenic shock tube, *J. Fluid Mech*, **66**, 177-187.

[9] Bai X, Avital EJ, Munjiza A, Williams JJR (2014) Numerical simulation of a marine current turbine in free surface flow, *Ren. Energy* **63**, 715-723.

[10] Toro EF (2009), *Riemann solvers and numerical methods for fluid dynamics, a practical introduction*, Springer.

[11] Rudinger G (1955), *Wave diagrams for unsteady flow in ducts*, D.Van Nostrand Company.

[12] Poinsot TJ and Lele SK (1992), Boundary conditions for direct simulations of compressible viscous flow, *J. Comp. Phys* **101**, 104-129.

[13] Yeh GKC and Kukl AL (1984), *Conservation equations for a non steady flow of a compressible viscous single-phase fluid in various coordinate systems*, DNA-TR-86-92.

[14] Avital EJ, Musafir RE and Korakianitis T (2013) Nonlinear propagation of sound emitted by high speed wave packets, *J Comp Acous* **21**(02), 1250027.

[15] Whitham GB (1973), *Linear and nonlinear waves*, Wiley.

List of figures:

Figure 1: Schematic description of the compression system

Figures 2: Verification case of a shock tube ; (a) schematic description of the shock tube at t =0 and (b) instantaneous pressure distributions in the shock shock tube that are plotted at t= 0.01 s

Figure 3: Verification case of a detached bow shock wave over a flat-faced cylinder at ambient sea level conditions and incoming M=2, where Mach number contour levels are shown

Figure 4: Geometry of the compression system at the x-r plane as it is laid out for the configurations of (a) uniform duct's cross-section area, (b) uniform duct's cross-section area with trimming at the end of the spherical duct to zero width, and (c) uniform duct's width.

Figure 5: Instantaneous pressure distributions that were simulated using the quasi-1D flow formulation and for the geometry configurations of Figs 4.

Figure 6: Instantaneous Mach number distributions that were simulated using the quasi-1D flow formulation and for the geometry configurations of Figs 4.

Figure 7: Pressure time history distributions that were simulated using the quasi-1D flow formulation and for the geometry configurations of Figs 4.

Figure 8: Pressure time history at selected points along the spherical duct, which was simulated using the quasi-1D flow formulation and for the geometry configurations of Figs 4.

Figure 9: The computational grid used for the axisymmetric simulation, where for clarity only one of ten grid points in the streamwise and stream normal directions are shown. The investigated geometries are for (a) uniform cross section area and (b) uniform cross section area but with trimming of the spherical duct width to 15% at its end.

Figure 10: Instantaneous pressure contours at times (a) 0.001, (b) 0.002 and (c) 0.003 s, which were simulated using the axisymmetric flow formulation for Geometry (a) of Fig 9.

Figure 11: Instantaneous pressure contours at times (a) 0.001, (b) 0.002 and (c) 0.003 s, which were simulated using the axisymmetric flow formulation for Geometry (b) of Fig 9.

Figure 12: Instantaneous Mach number contours at times (a) 0.001, (b) 0.002 and (c) 0.003 s, which were simulated using the axisymmetric flow formulation for Geometry (a) of Fig 9.

Figure 13 Instantaneous Mach number contours at times (a) 0.001, (b) 0.002 and (c) 0.003 s, which were simulated using the axisymmetric flow formulation for Geometry (b) of Fig 9.

Figure 14 Pressure time history distributions along the system's axis of symmetry at the tube region and inner wall at other regions that were simulated using the axisymmetric flow formulation and for the geometry configurations of Figs 9.

Figure 15: Pressure time history at selected points along the spherical duct's inner wall, which was simulated using the axisymmetric flow formulation and for the geometry configurations of Figs 9.

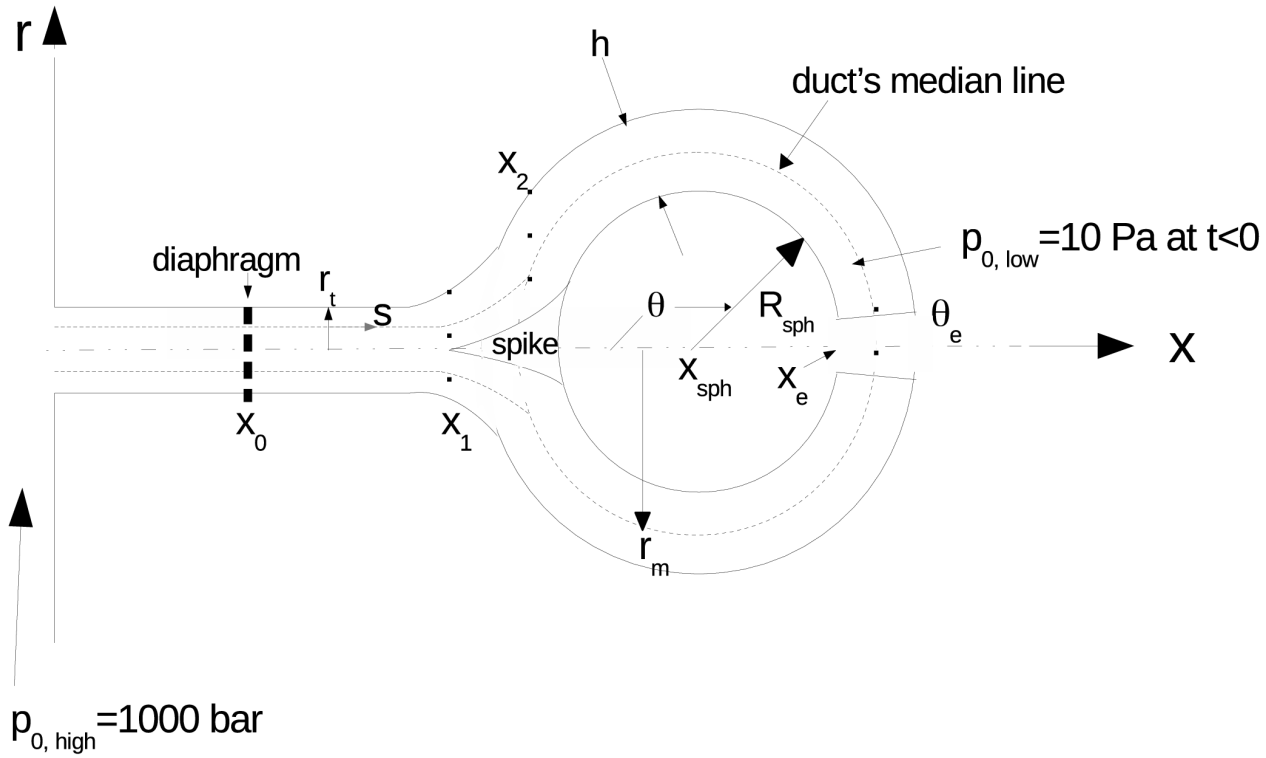

Figure 1: Schematic description of the compression system

(a)

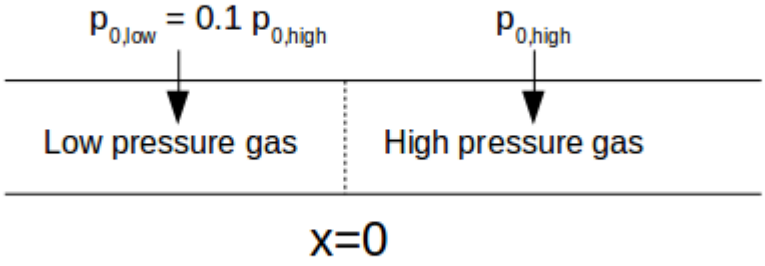

(b)

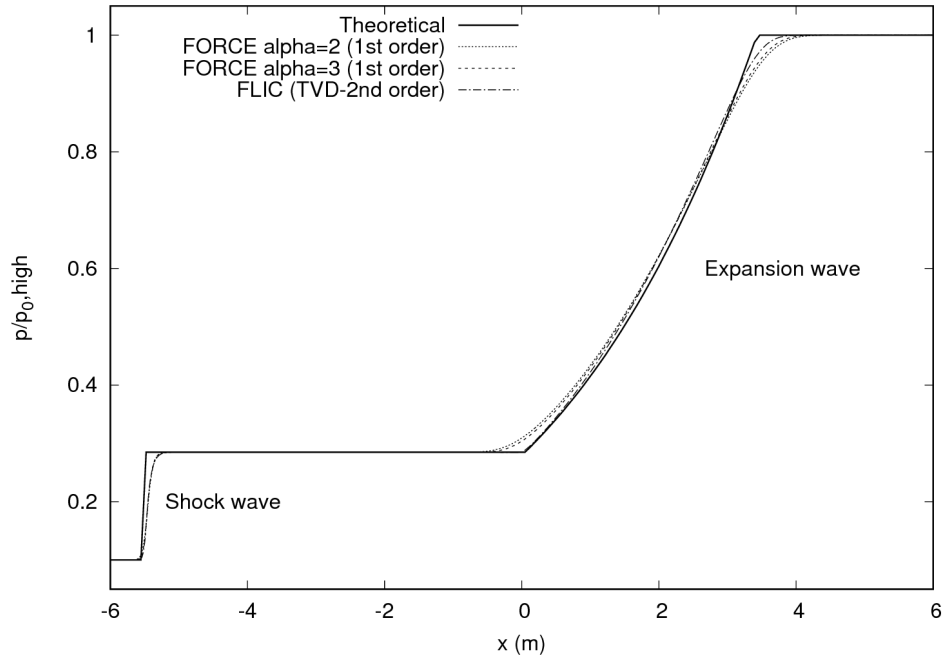

Figures 2: Verification case of a shock tube ; (a) schematic description of the shock tube at t =0 and (b) instantaneous pressure distributions in the shock shock tube that are plotted at t= 0.01 s

476

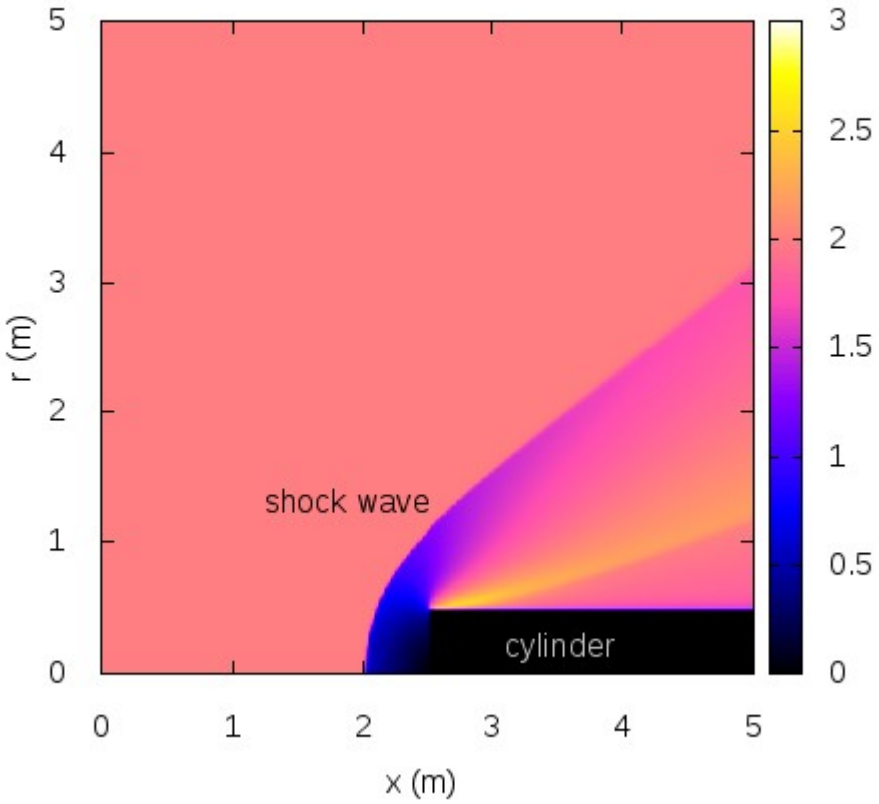

Figure 3: Verification case of a detached bow shock wave over a flat-faced cylinder at ambient sea level conditions and incoming M=2, where Mach number contour levels are shown

477

(a)

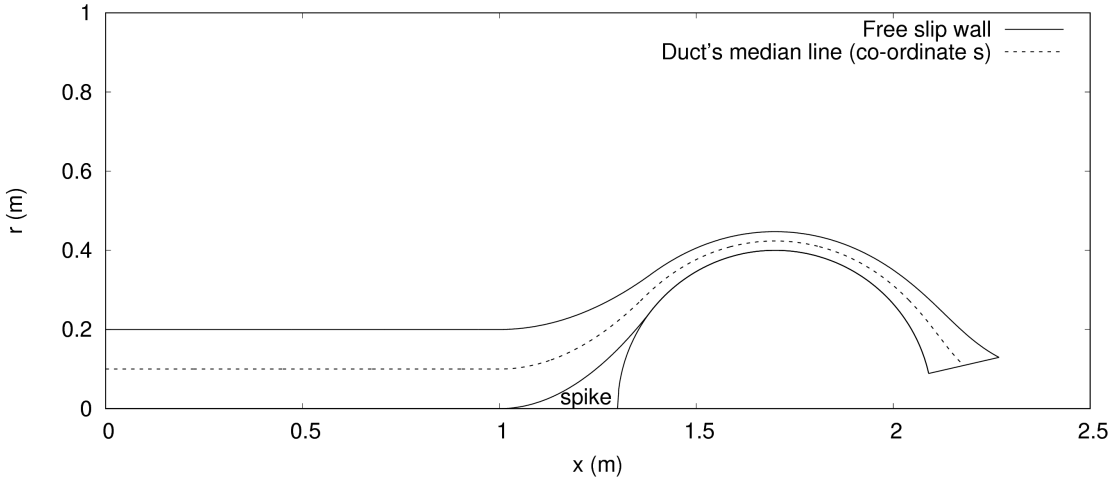

(b)

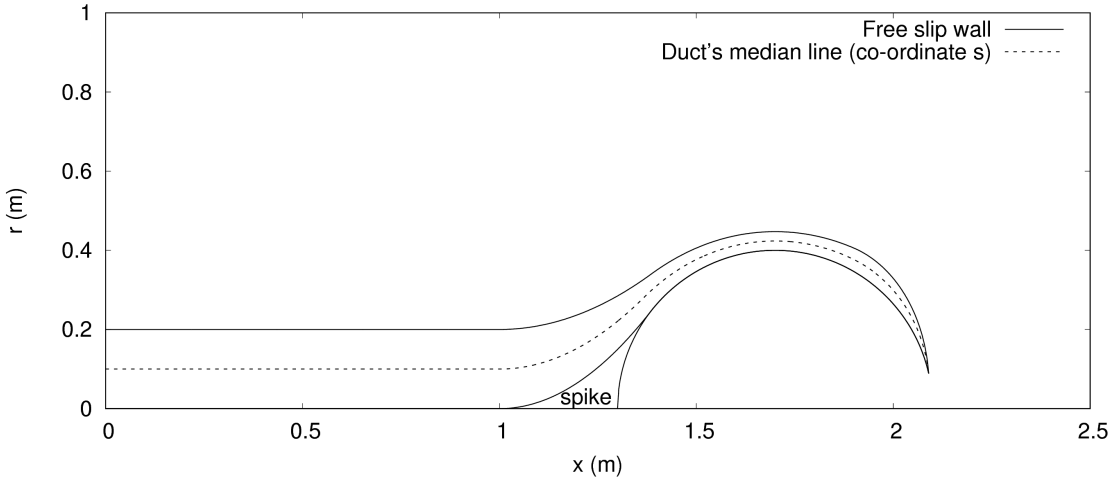

(c)

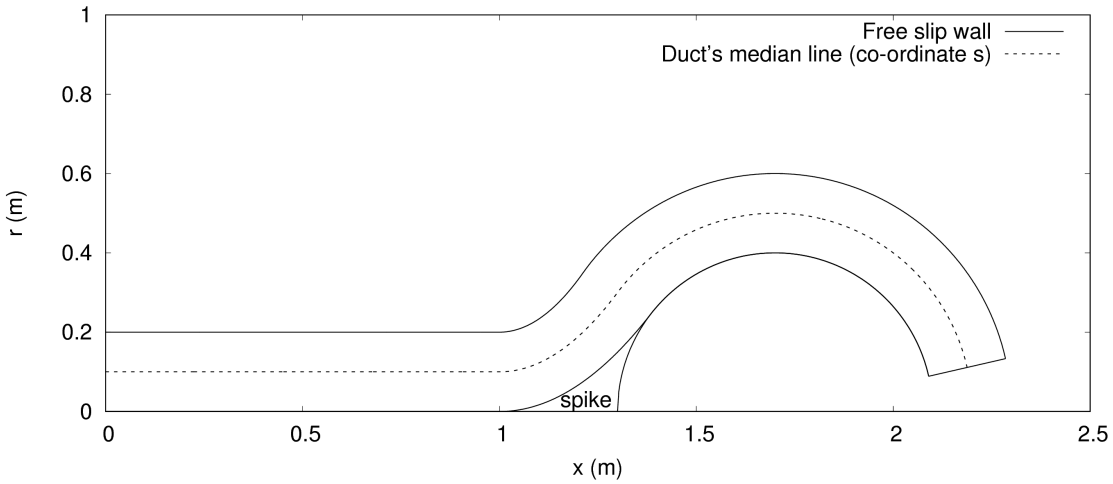

Figure 4: Geometry of the compression system at the x-r plane as it is laid out for the configurations of (a) uniform duct's cross-section area, (b) uniform duct's cross-section area with trimming at the end of the spherical duct to zero width, and (c) uniform duct's width.

(a)

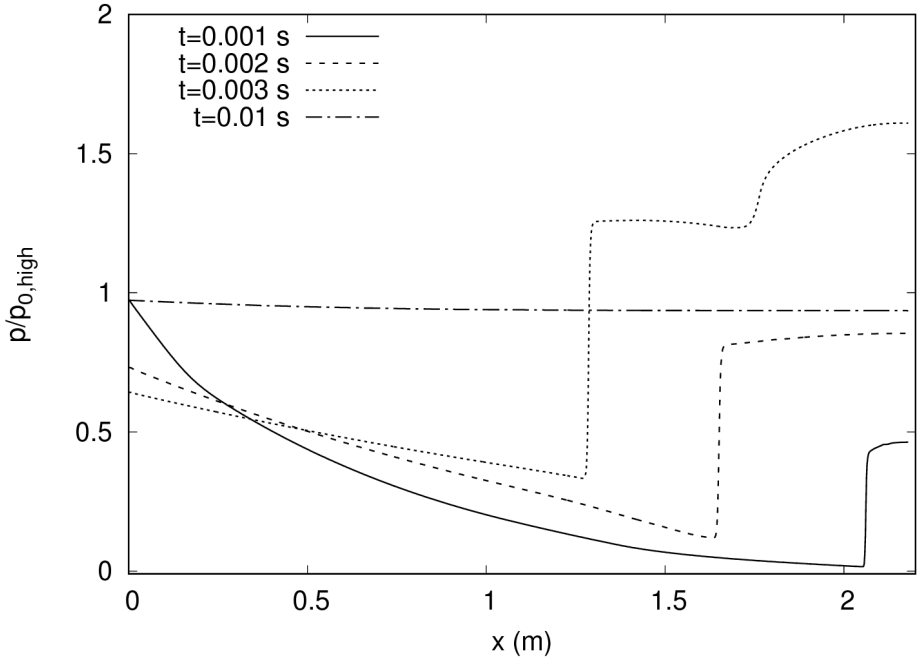
t=0.001 s
t=0.002 s
t=0.003 s
t=0.01 s
p/p0,high
x (m)
0
0.5
1
1.5
2

(b)

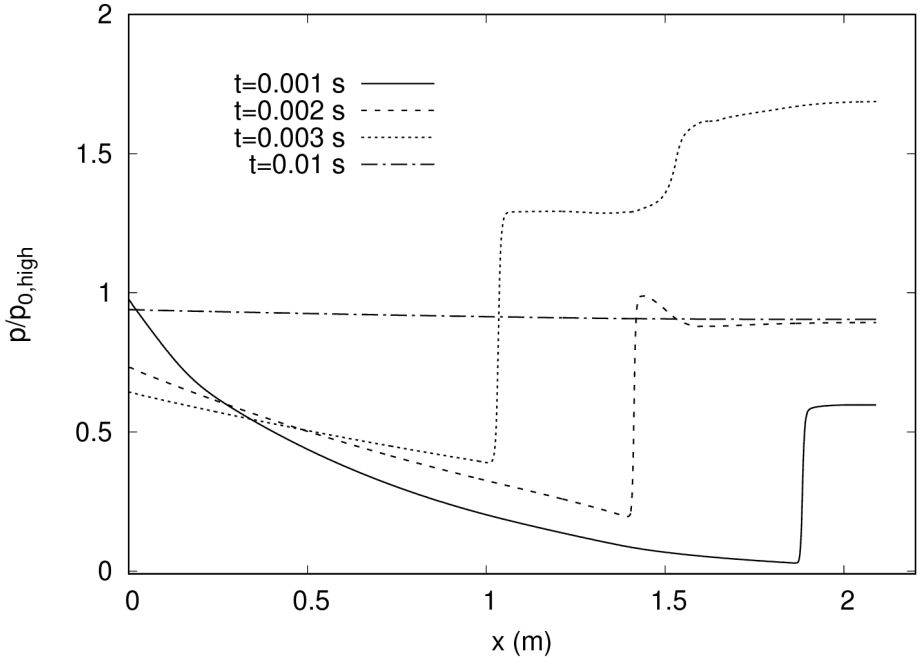
t=0.001 s
t=0.002 s
t=0.003 s
t=0.01 s
p/p0,high
x (m)
0
0.5
1
1.5
2

481

(c)

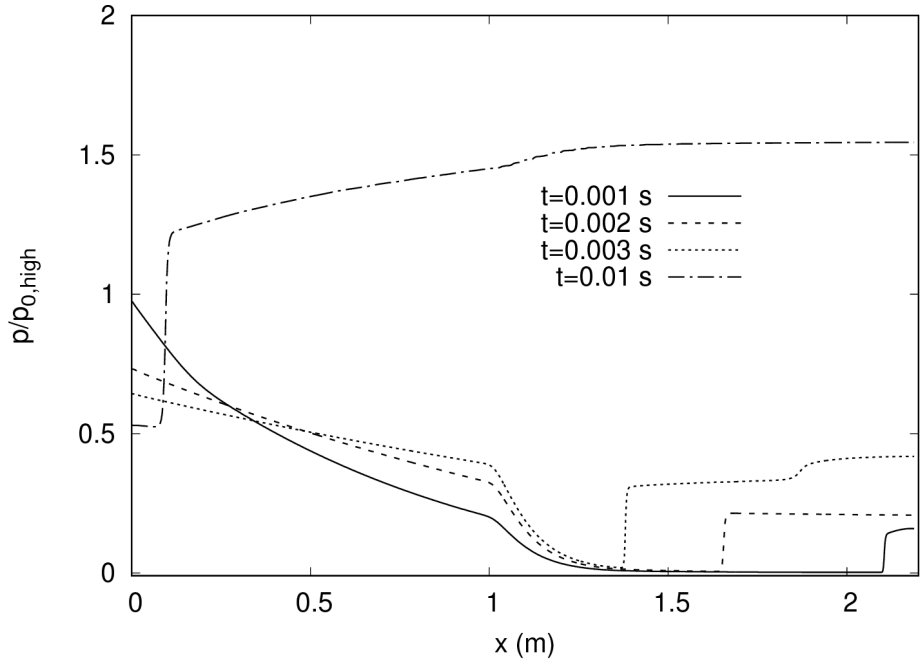

Figure 5: Instantaneous pressure distributions that were simulated using the quasi-1D flow formulation and for the geometry configurations of Figs 4.

(a)

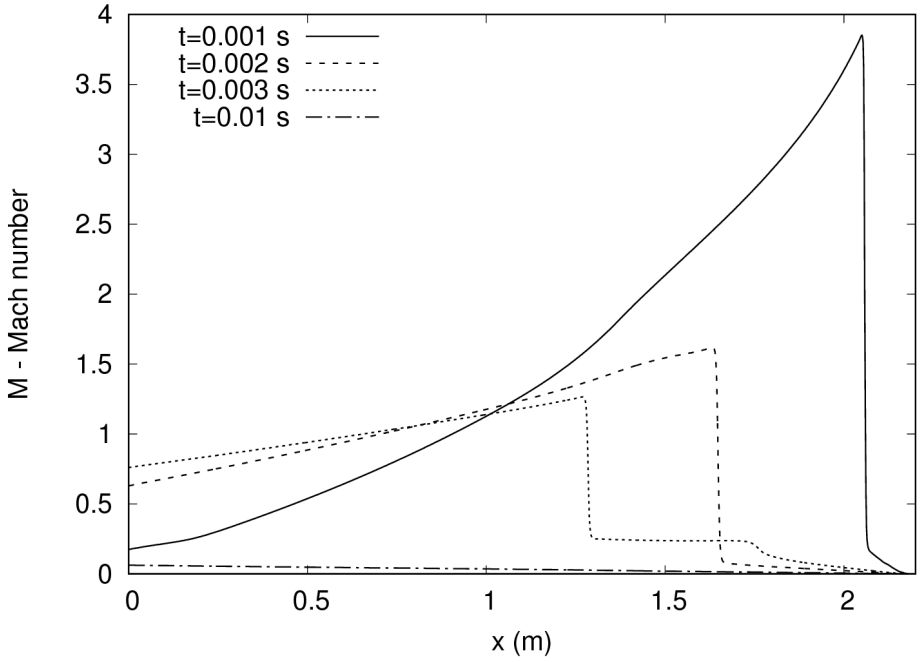
t=0.001 s
t=0.002 s
t=0.003 s
t=0.01 s
M - Mach number
x (m)
0
0.5
1
1.5
2
2.5
3
3.5
4

(b)

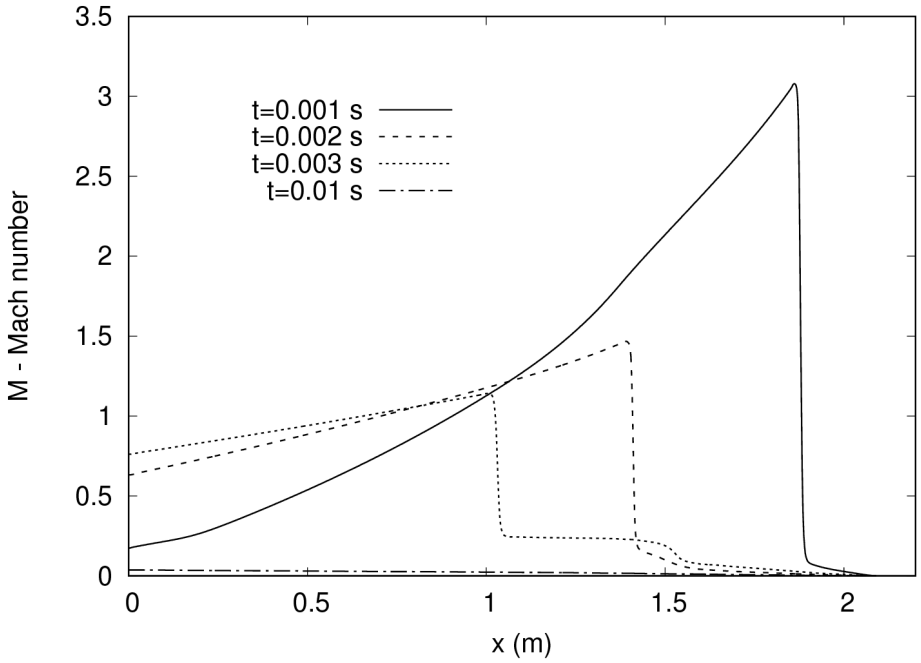
t=0.001 s
t=0.002 s
t=0.003 s
t=0.01 s
M - Mach number
x (m)
0
0.5
1
1.5
2
2.5
3
3.5

485

(c)

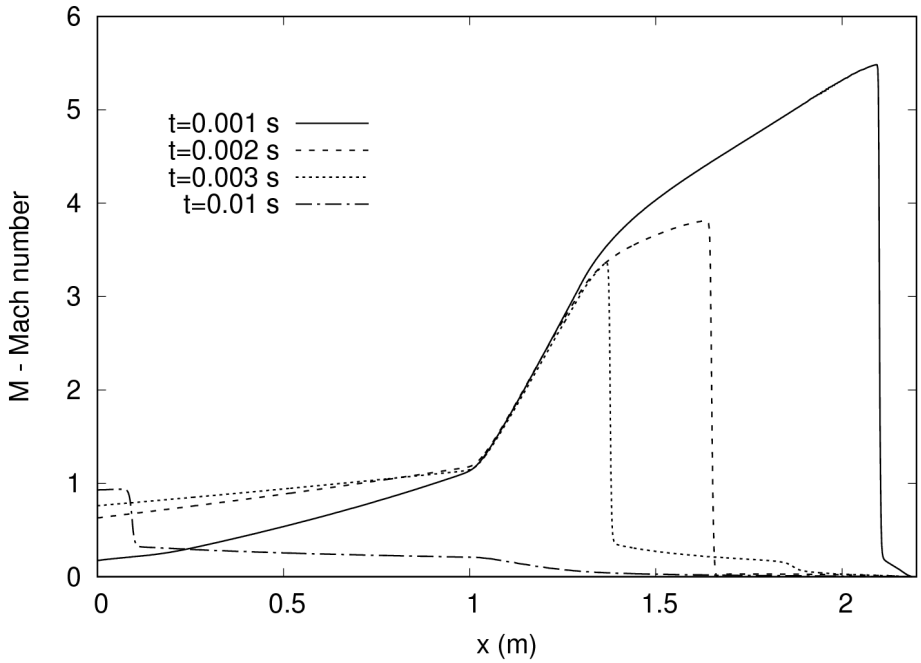

Figure 6: Instantaneous Mach number distributions that were simulated using the quasi-1D flow formulation and for the geometry configurations of Figs 4.

(a)

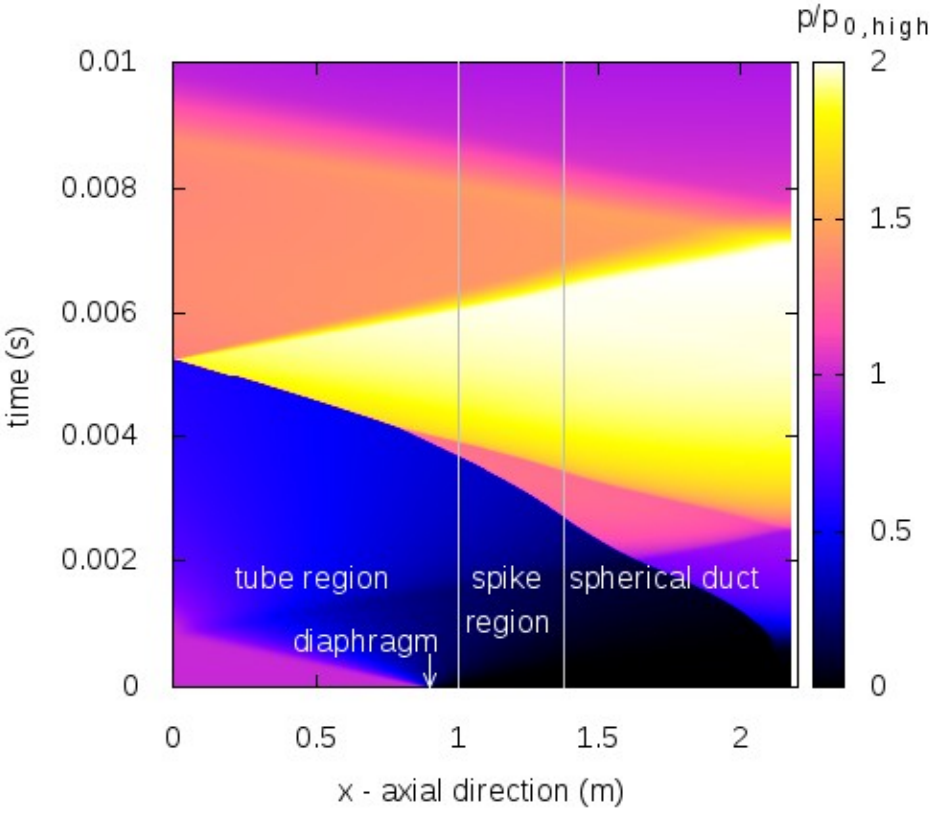
p/p0,high
2
1.5
1
0.5
0
0.01
0.008
0.006
0.004
0.002
0
time (s)
tube region
spike region
spherical duct
diaphragm
0
0.5
1
1.5
2
x - axial direction (m)

(b)

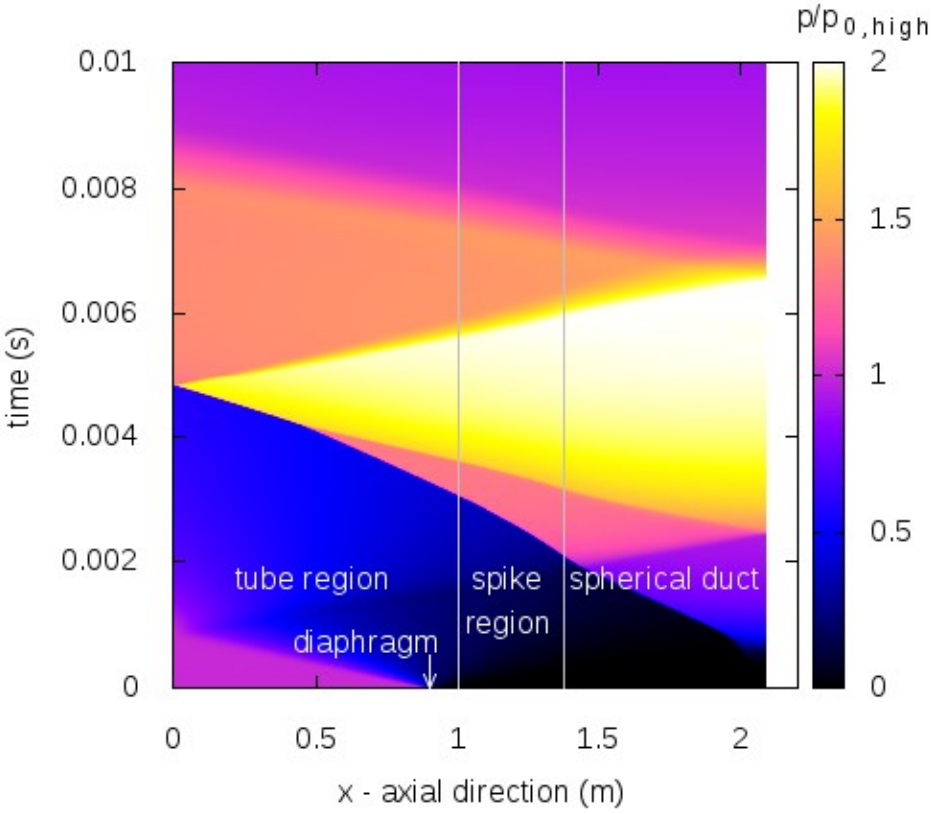
p/p0,high
2
1.5
1
0.5
0
0.01
0.008
0.006
0.004
0.002
0
time (s)
tube region
spike region
spherical duct
diaphragm
0
0.5
1
1.5
2
x - axial direction (m)

(c)

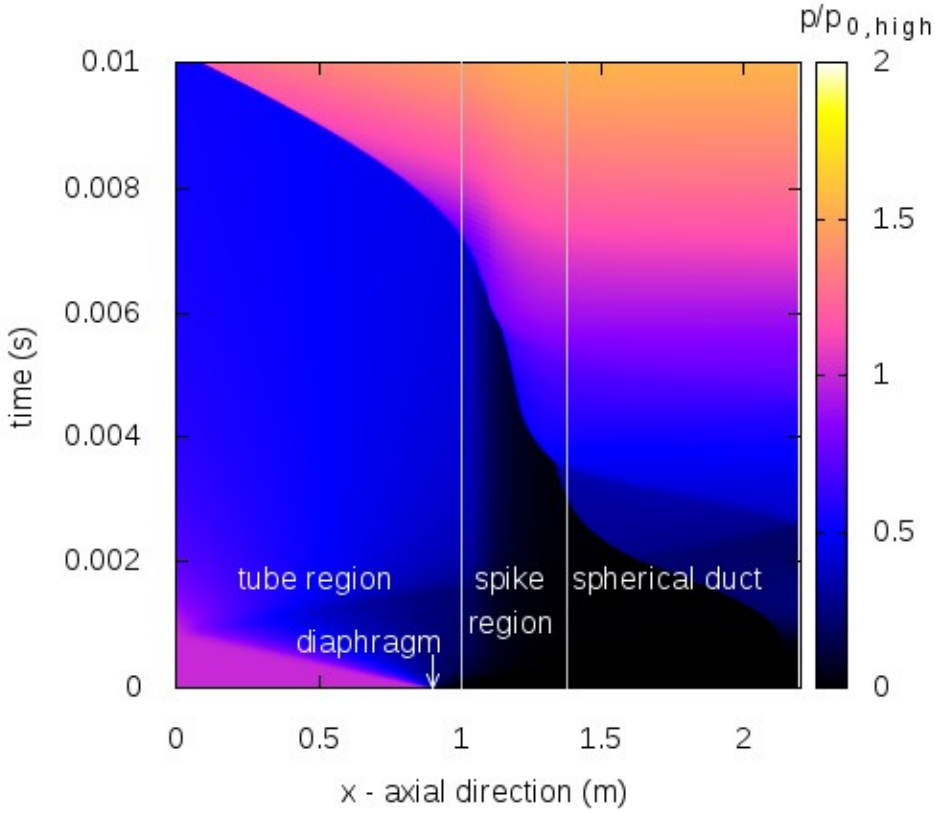

Figure 7: Pressure time history distributions that were simulated using the quasi-1D flow formulation and for the geometry configurations of Figs 4.

(a)

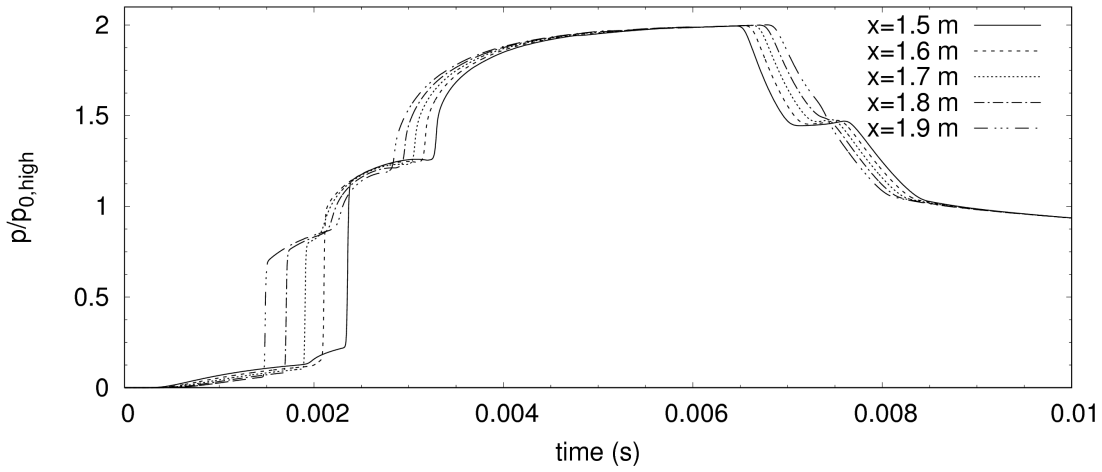

(b)

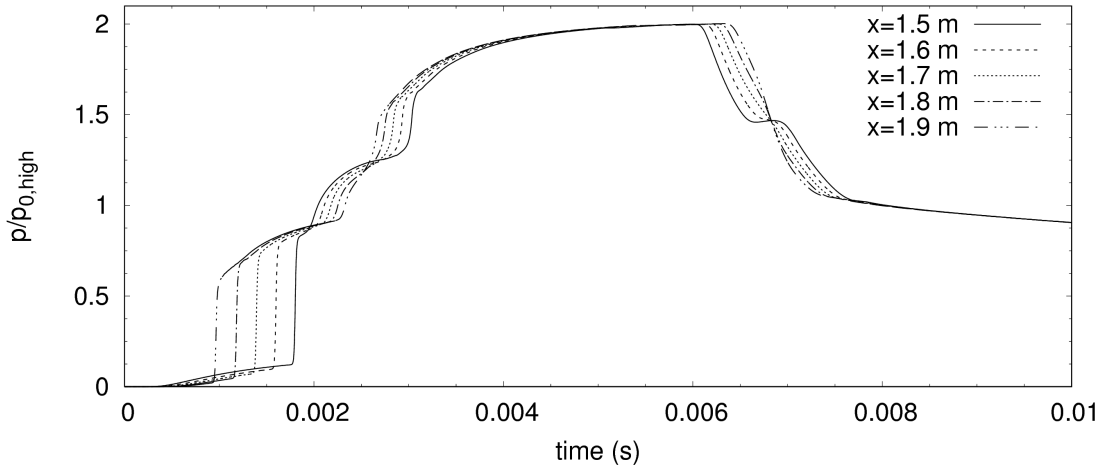

(c)

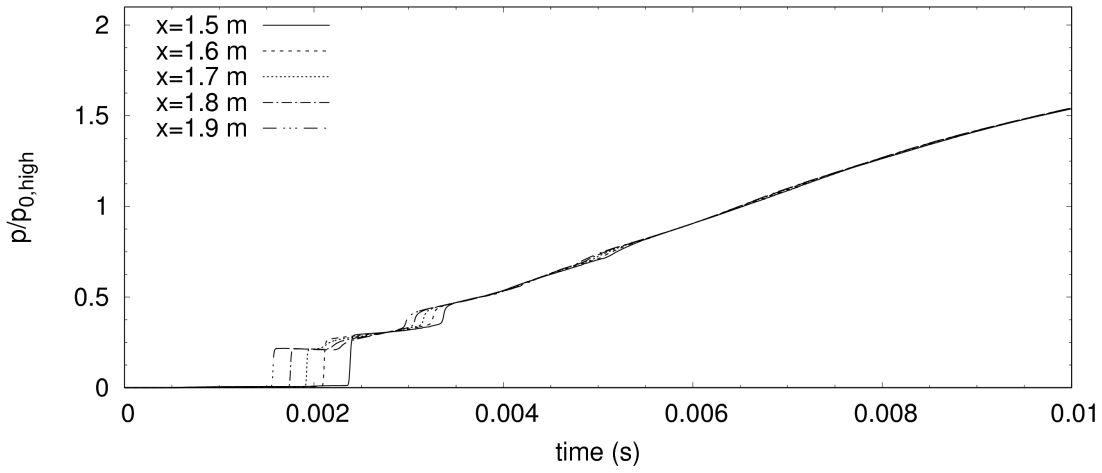

Figure 8: Pressure time history at selected points along the spherical duct, which was simulated using the quasi-1D flow formulation and for the geometry configurations of Figs 4.

(a)

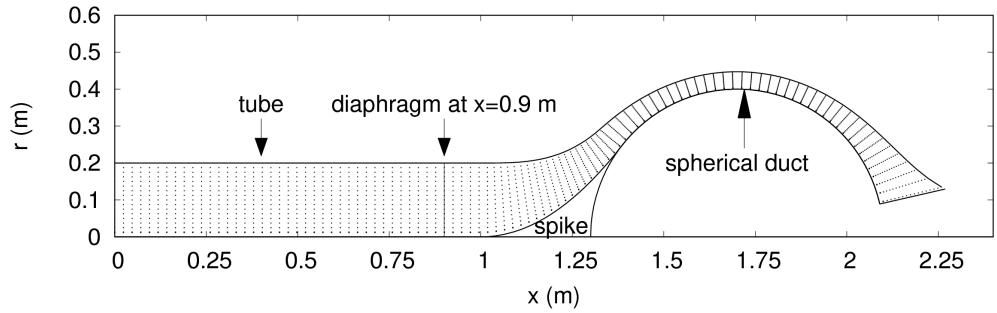

(b)

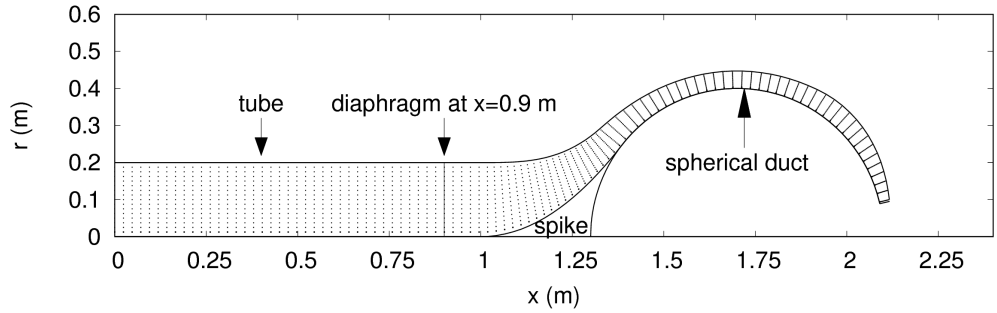

Figure 9: The computational grid used for the axisymmetric simulation, where for clarity only one of ten grid points in the streamwise and stream normal directions are shown. The investigated geometries are for (a) uniform cross section area and (b) uniform cross section area but with trimming of the spherical duct width to 15% at its end.

(a)

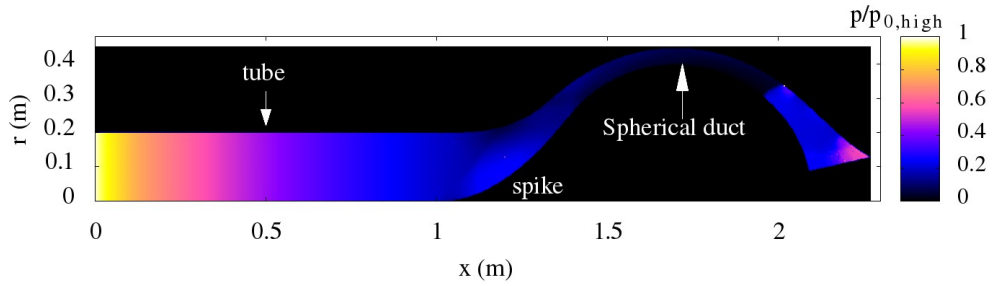

(b)

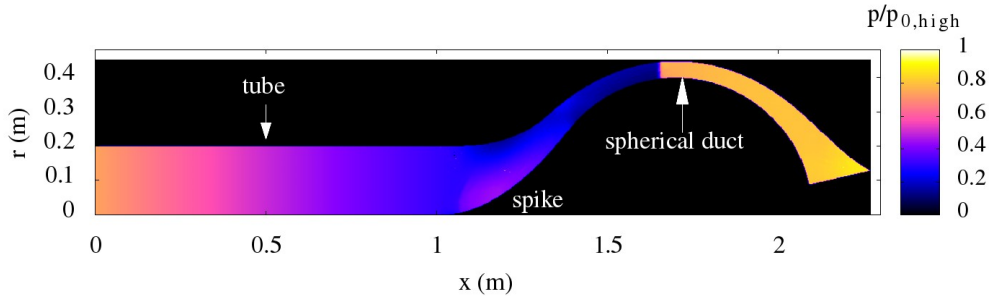

(c)

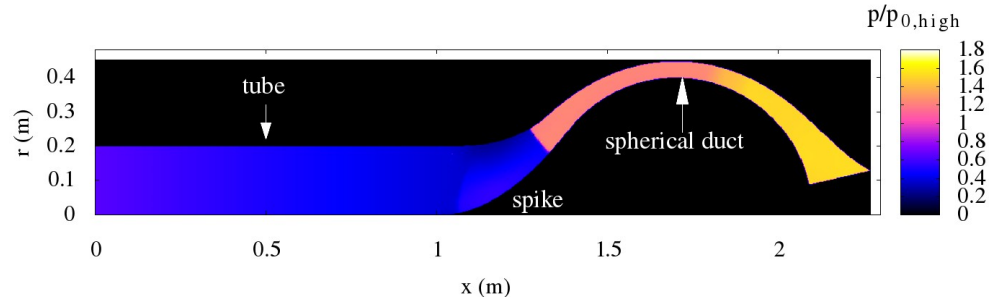

Figure 10: Instantaneous pressure contours at times (a) 0.001, (b) 0.002 and (c) 0.003 s, which were simulated using the axisymmetric flow formulation for Geometry (a) of Fig 9.

(a)

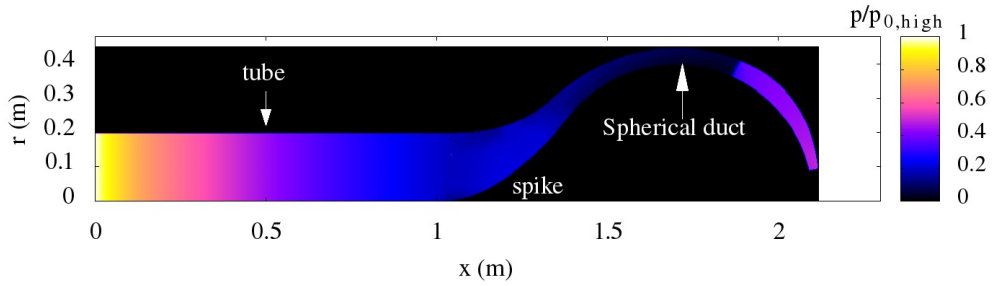

(b)

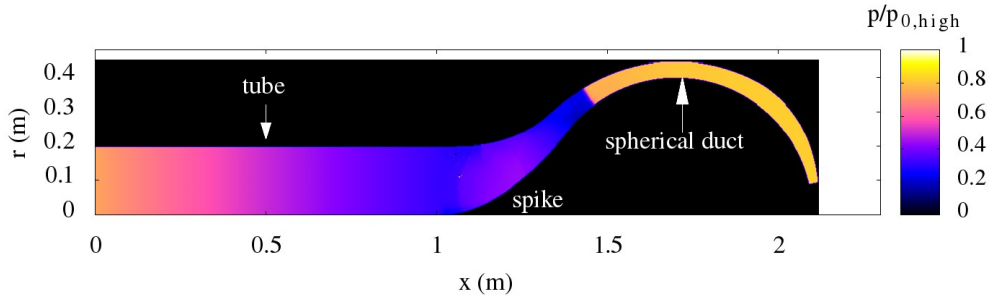

(c)

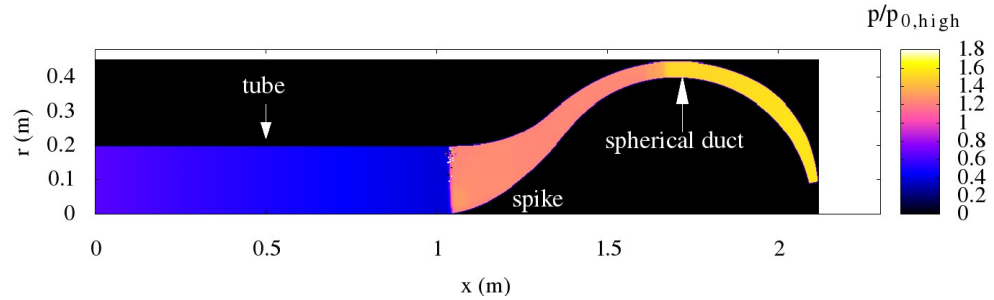

Figure 11: Instantaneous pressure contours at times (a) 0.001, (b) 0.002 and (c) 0.003 s, which were simulated using the axisymmetric flow formulation for Geometry (b) of Fig 9.

(a)

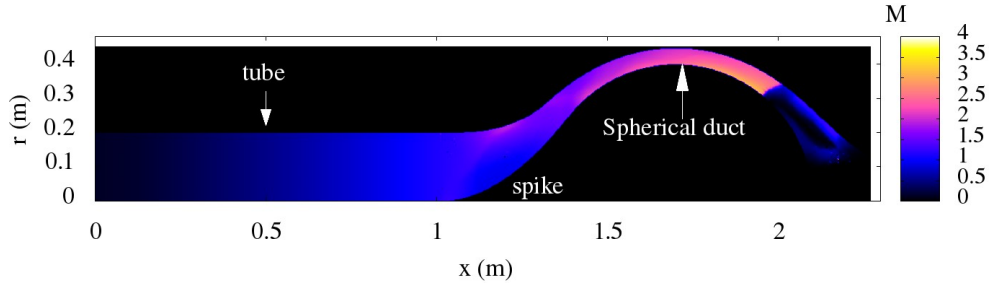

(b)

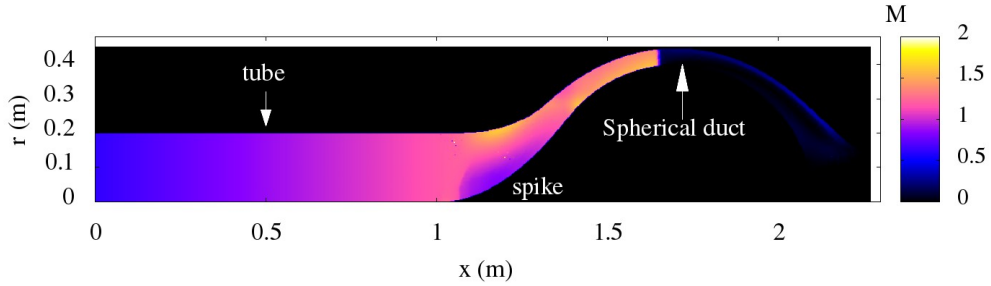

(c)

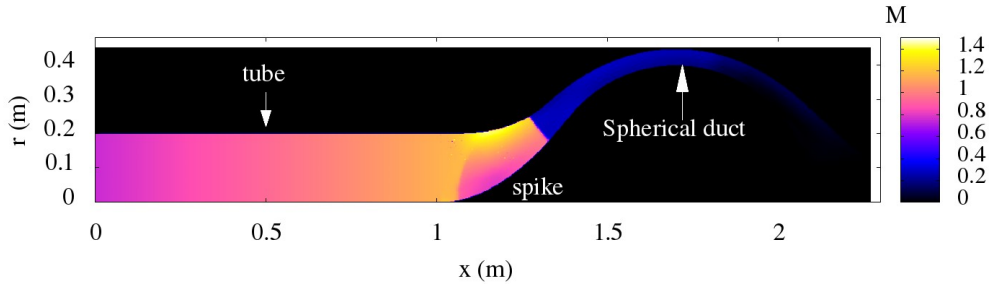

Figure 12: Instantaneous Mach number contours at times (a) 0.001, (b) 0.002 and (c) 0.003 s, which were simulated using the axisymmetric flow formulation for Geometry (a) of Fig 9.

(a)

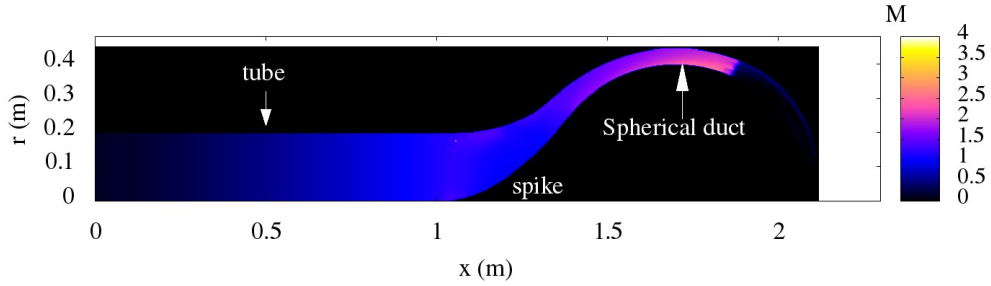

(b)

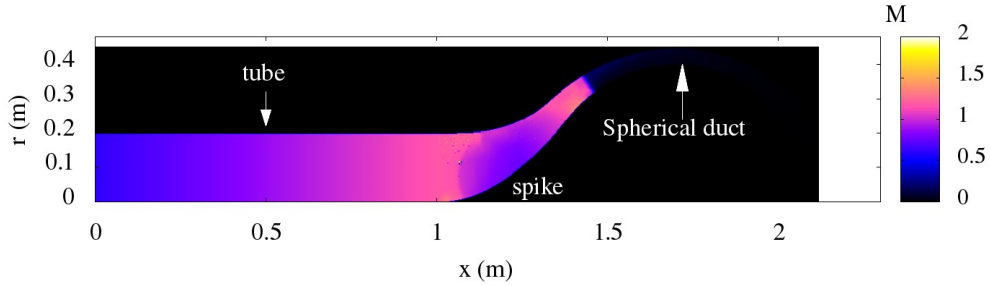

(c)

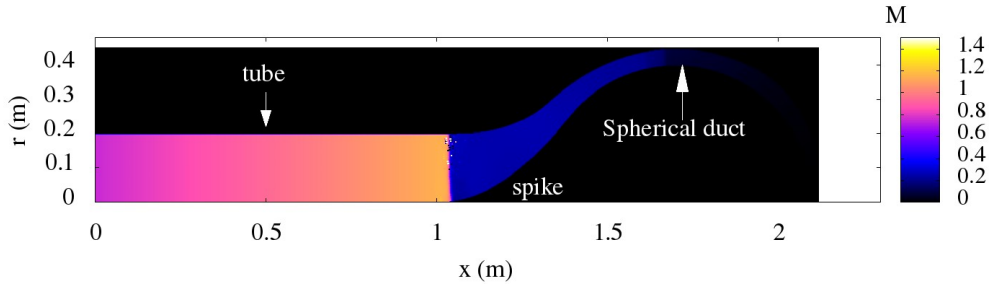

Figure 13 Instantaneous Mach number contours at times (a) 0.001, (b) 0.002 and (c) 0.003 s, which were simulated using the axisymmetric flow formulation for Geometry (b) of Fig 9.

510

14(a)

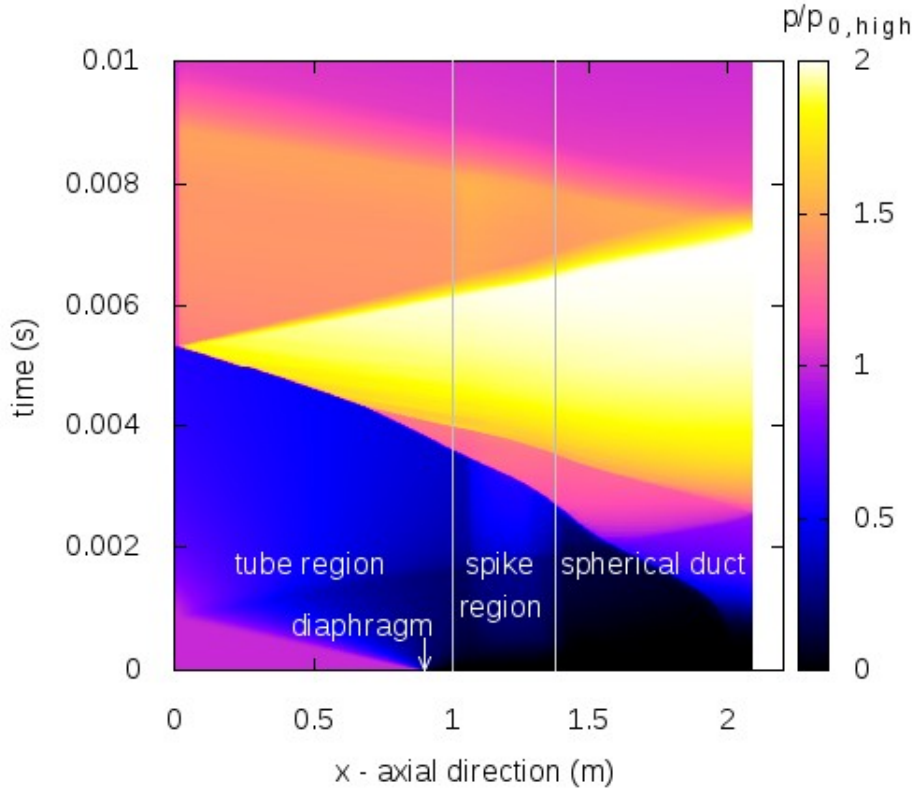
p/p0,high
2
1.5
1
0.5
0
0.01
0.008
0.006
0.004
0.002
0
time (s)
tube region
spike region
spherical duct
diaphragm
0
0.5
1
1.5
2
x - axial direction (m)

14(b)

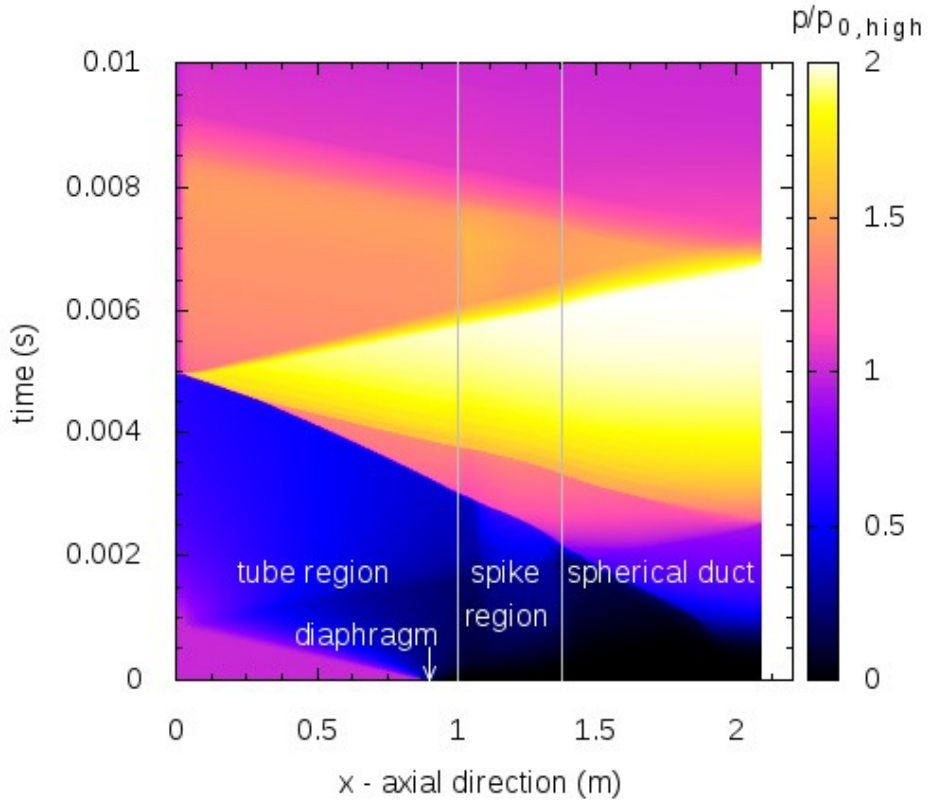

Figure 14: Pressure time history distributions along the system's axis of symmetry at the tube region and inner wall at other regions that were simulated using the axisymmetric flow formulation and for the geometry configurations of Figs 9.

514

15 (a)

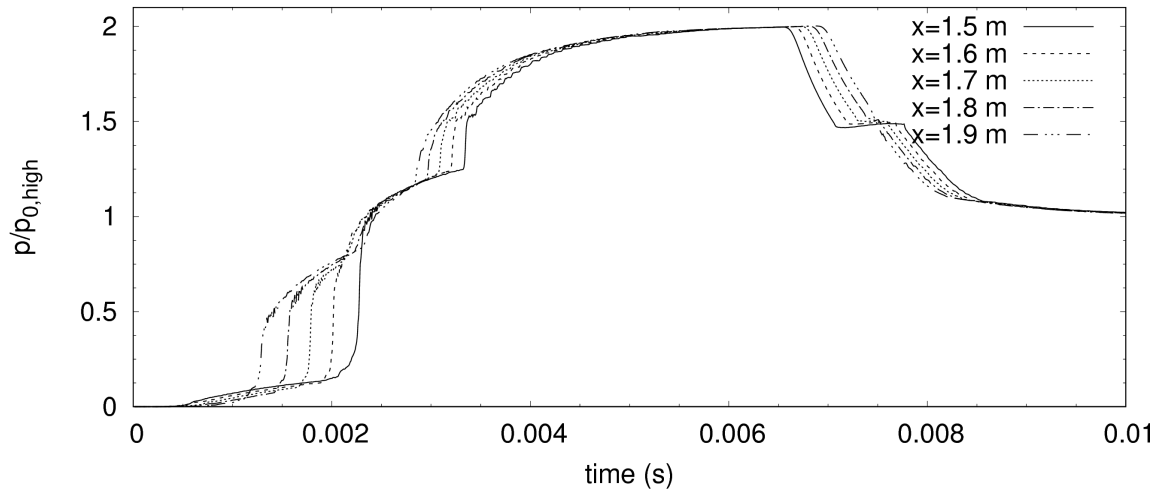

15 (b)

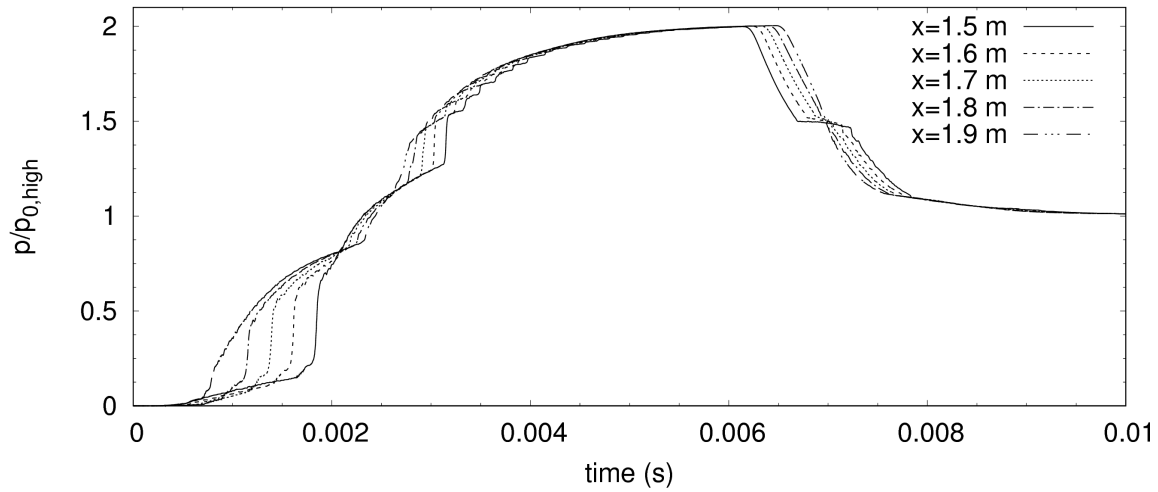

515 Figure 15: Pressure time history at selected points along the spherical duct's inner wall, which was
516 simulated using the axisymmetric flow formulation and for the geometry configurations of Figs 9.

Appendix A - Spike duct's grid streamwise line design.

Following the schematics shown in Figure 1, we will normalize x and r by R_{sph} as follows

$$\tilde{x}=x/R_{sph}\ ,\ \ \tilde{r}=r/R_{sph}\ \ . \tag{A1}$$

A simple geometric variation of the grid line can be written as a second order polynomial;

$$\tilde{r}_m=a_0+a_1(\tilde{x}-\tilde{x}_1)+a_2(\tilde{x}-\tilde{x}_1)^2\ ,\ \ \tilde{x}_1\leqslant\tilde{x}\leqslant\tilde{x}_2\ \ . \tag{A2}$$

At the junction of the spike's duct grid streamwise line with the straight tube's streamwise grid line $x = x_1$, see Figure 1 we require

$$\tilde{r}_m=\beta R_t/R_{sph}=\beta\tilde{R}_t\ ,\ \ d\tilde{r}_m/d\tilde{x}=0\ \ . \tag{A3}$$

$0\leq\beta\leq1$ and β= (0, 0.5, 1) corresponds to the inner wall (or axis of symmetry for the tube), median line s and outer wall of the duct respectively. At the junction of the spike duct's streamwsie line with the spherical duct's streamwise line $x = x_2$, we require

$$\tilde{r}_m=(1+\beta\tilde{h})\sin\theta_2\ \ , \tag{A4.1}$$

$$\frac{d\tilde{r}_m}{d\tilde{x}}=\beta\frac{d\tilde{h}}{d\tilde{x}}\sin\theta_2+(1+\beta\tilde{h})\cos\theta_2\frac{d\theta}{d\tilde{x}}\ \ , \tag{A4.2}$$

where

$$(1+\beta\tilde{h})\cos\theta_2=\tilde{x}_{sph}-\tilde{x}_2\ \ . \tag{A5}$$

θ is the spherical angle, see Figure 1.

From Eqs. (A3) one gets $a_0=\beta R_t/R_{sph}$ and $a_1=0$. We will denote $d\tilde{h}/d\theta=G$, where G=0 for a constant spherical duct's width - h_0. For a constant cross-section area A_0 of the spherical duct, one gets after using the result of Appendix B;

$$G=\frac{-\tilde{A}_0\cos\theta}{2\pi\sin^2\theta\sqrt{1+\dfrac{\tilde{A}_0}{\pi\sin\theta}}}\ \ , \tag{A6}$$

where $\tilde{A}_0=A_0/R_{sph}^2$. Using Eq. (A5) one gets

$$\frac{d\theta}{d\tilde{x}}=\frac{1}{(1+\beta\tilde{h})\sin\theta-\beta G\cos\theta}\ \ . \tag{A7}$$

Substituting Eq. (A7) into Eq. (A4.2) leads to;

$$\frac{d\tilde{r}_m}{d\tilde{x}}=\frac{\beta G(\theta_2)\sin\theta_2+(1+\beta\tilde{h})\cos\theta_2}{(1+\beta\tilde{h})\sin\theta_2-\beta G(\theta_2)\cos\theta_2}\ \ . \tag{A8}$$

However from Eqs. (A2) & (A3) one also gets;

$$\widetilde{r}_m = \beta \widetilde{R}_t + a_2 (\widetilde{x}_2 - \widetilde{x}_1)^2 \quad , \tag{A9.1}$$

$$d\widetilde{r}_m / d\widetilde{x} = 2 a_2 (\widetilde{x}_2 - \widetilde{x}_1) \quad . \tag{A9.2}$$

Eq. (A9.1) must be equal to Eq. (A 4.1) and Eq. (A9.2) must be equal to Eq. (A8) leading to;

$$\beta \widetilde{R}_t + a_2 (\widetilde{x}_2 - \widetilde{x}_1)^2 = (1 + \beta \widetilde{h}) \sin\theta_2 \quad , \tag{A10.1}$$

$$2 a_2 (\widetilde{x}_2 - \widetilde{x}_1) = \frac{\beta G(\theta_2) \sin\theta_2 + (1 + \beta \widetilde{h}) \cos\theta_2}{(1 + \beta \widetilde{h}) \sin\theta_2 - \beta G(\theta_2) \cos\theta_2} \quad . \tag{A10.2}$$

For given duct's width h and the axial location of the start of the spike's zone x_1, Eqs. (A10) and (A5) form a closed set of non-linear equations for the unknowns a_2, x_2 and θ_2. This can be solved using the false position method for the unknown θ_2. One should note that a_2, x_2 and θ_2 generally depend β, i.e. the distance of the streamwise grid line from the duct's inner wall.

Appendix B – Variation of the spherical duct's width for a constant cross-section area and trimming its end

Following the schematics shown in Figure 1 one gets the following relation between the duct's width h and its cross-section area A:

$$2\pi (R_{sph} + 0.5h) \sin\theta \; h = A \quad . \tag{B1}$$

Normalizing all spatial lengths by R_{sph} as in Appendix A and denoting A_0 as the constant cross-section area of the spherical duct yields;

$$\widetilde{h} = \sqrt{1 + \frac{\widetilde{A}_0}{\pi \sin\theta}} - 1 \quad , \tag{B2}$$

where $\widetilde{h} = h / R_{sph}$, $\widetilde{A}_0 = A_0 / R_{sph}^2$.

The trimming of the spherical duct's end is achieved as follows;

$$h_t = h\left[1 - \beta_{trim} (x - x_t)^2 / (x_e - x_t)^2\right] , 0 \leqslant \beta_{trim} \leqslant 1, \;\; x_t \leqslant x \leqslant x_e \quad , \tag{B3}$$

where h is the duct's width that should have been without the trimming, x_t is the axial location of the start of trimming and x_e is at the end of the trimmed duct. β_{trim} controls the amount of trimming, when it is zero there is no trimming and when β_{trim} is one the end of the spherical duct is fully trimmed to zero width.